Preprint typeset in JINST style - HYPER VERSION

R&D for Very Forward Calorimeters at the ILC Detector

First Author[a], Second Author[b*] and Third Author[b]

[a]*Name of Institute,*
Address, Country
[b]*Name of Institute,*
Address, Country
E-mail: `Wolfgang.Lohmann@desy.de`

ABSTRACT: Special calorimeters are needed to instrument the very forward region of an ILC detector. These devices will improve the hermeticity being important for new particle searches. A luminometer is foreseen to measure the rate of low angle Bhabha scattering with a precision better than 10^{-3}. A calorimeter adjacent to the beam-pipe will be hit by a large amount of beamstrahlung remnants. The amount and shape of these depositions will allow a fast luminosity estimate and the determination of beam parameters. However, the sensors must be extremely radiation hard. Finely segmented and very compact calorimeters will match the requirements. Due to the high occupancy fast FE electronics is needed. A possible design of the calorimeters is presented and an overview on the R&D status is given.

KEYWORDS: Forward Calorimeters, ILC Detector, Luminosity Measurement .

*Corresponding author.

Contents

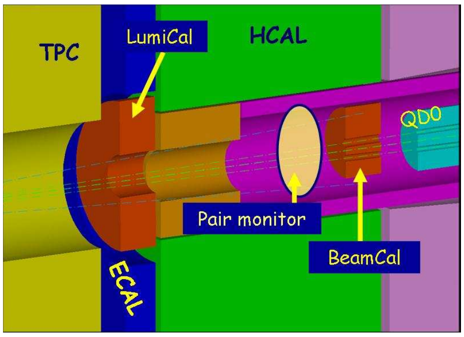

Figure 1. The very forward region of the ILD detector. LumiCal, BeamCal, Pair Monitor, and QD0 are carried by the support tube. TPC denotes the central track chamber, ECAL the electromagnetic and HCAL the hadron calorimeter.

1. The Challenges

Two calorimeters are foreseen in the very forward region of the ILC detector near the interaction point - LumiCal for the precise measurement of the luminosity and BeamCal for the fast estimate of the luminosity [1] and to control beam parameters. Both will improve the hermeticity of the detector. To support beam-tuning a pair monitor is foreseen, positioned just in front of BeamCal.

LumiCal will measure the luminosity using as gauge process Bhabha scattering, $e^+e^- \to e^+e^-(\gamma)$. To match the physics benchmarks, an accuracy of better than 10^{-3} is needed. For the GigaZ option even an accuracy of 10^{-4} is aimed [2]. Hence, LumiCal is a precision device with challenging requirements on the mechanics and position control. All detectors in the very forward region have to tackle relatively high occupancies, requiring special FE electronics.

BeamCal is positioned just outside the beam-pipe. A large amount of low energy electron-positron pairs originating from beamstrahlung will deposit their energy in BeamCal. These depositions, useful for a bunch-by-bunch luminosity estimate and the determination of beam parameters [3], will lead, however, to a radiation dose of several MGy per year in the sensors at lower polar angles. Hence extremely radiation hard sensors are needed to instrument BeamCal. A pair monitor, consisting of a layer of pixel sensors positioned just in front of BeamCal, will measure the density of beamstrahlung pairs and give additional information for beam parameter determination.

A small Moliere radius is of invaluable importance for both calorimeters. It ensures an excellent electron veto capability for BeamCal even at small polar angles, being essential to suppress background in new particle searches where the signatures are large missing energy and momentum. In LumiCal the precise reconstruction of electron and positron showers of Bhabha events is facilitated and background processes will be rejected efficiently.

2. The Design of the Very Forward Region

A sketch of the very forward region of the ILD detector, as an example, is shown in Figure 1. LumiCal and BeamCal are cylindrical electromagnetic calorimeters, centered around the outgoing beam. LumiCal is positioned inside and aligned with the forward electromagnetic calorimeter. BeamCal is placed just in front of the final focus quadrupole. BeamCal covers polar angles between 5 and 40 mrad and LumiCal between 31 and 77 mrad.

The colliding beams enter the interaction point, IP, with a crossing angle of 14 mrad. Both calorimeters are centered around the outgoing beam. In the design of BeamCal a hole for the incoming beam-pipe is foreseen.

2.1 Mechanics

LumiCal and BeamCal are designed as cylindrical sensor-tungsten sandwich calorimeters. Both consist of 30 absorber disks of 3.5 mm thickness, corresponding to one radiation length, interspersed with sensor layers. Front-end ASICs are positioned at the outer radius of the calorimeters.

To allow mounting when the beam-pipe is installed both calorimeters consist of two half-cylinders. A schematic of a half cylinder of BeamCal is shown in Figure 2a). The tungsten absorber

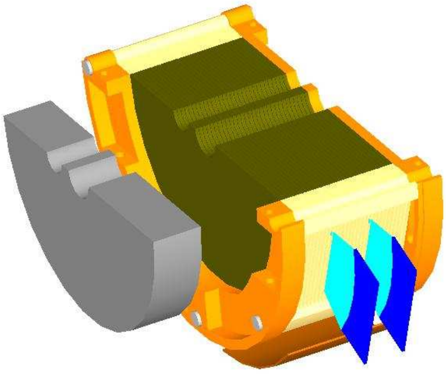

(a)

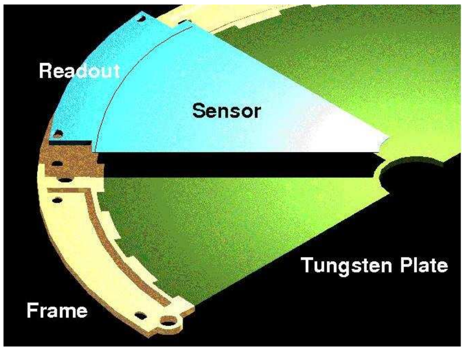

(b)

Figure 2. a) A half-cylinder of BeamCal. The brown block is the tungsten absorber structure interspersed with sensor layers. The orange structure represents the mechanical frame. The blue segments at the outer radius indicate the front-end electronics. In front of the calorimeter a graphite shield is shown in gray. b) A half-layer of an absorber disk assembled with a sensor sector and the front-end read-out.

disks are embedded in a mechanical frame stabilised by steel rods. Each layer is composed of the tungsten half-disc surrounded by a brass half-ring as shown in Figure 2b). Precise holes in the brass ring will ensure the necessary position accuracy. The sensors are fixed on the tungsten and connected via a flexible PCB to the front-end readout. The distance between two adjacent tungsten place is kept small to ensure a small Moliere radius.

The design of LumiCal is similar. Since it is a precision device special care is devoted to the mechanical stability and position control. The tungsten half-discs are hold by special bolts. For a half barrel structure as shown in Figure 3 a finite element simulation is performed. The calorimeter weight leads to a maximal vertical displacement of 21 μm (where??). For a temperature difference of one degree Celsius over a plane the deformation of the shape of a tungsten plate is estimated to be 25 μm.

2.2 Sensor Layers

For LumiCal sensors made of high ohmic n-type silicon are foreseen. The thickness of the sensors is about 300μm. The p$^+$ is segmented in polar and azimuthal pads and the backside is fully

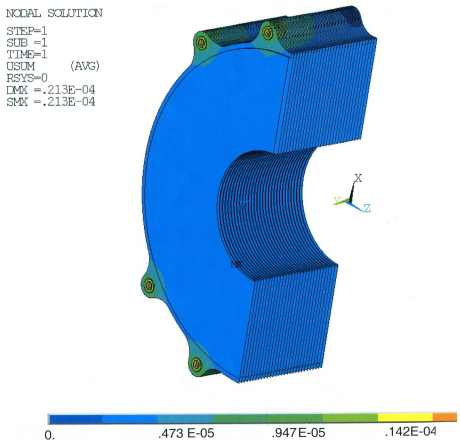

Figure 3. The mechanical structure of a half-cylinder of LumiCal. Tungsten disks are precisely positioned using 4 bolts which are stabilized by additional steel rings on both sides of the cylinder. Shown here is the result of a finite element calculation to estimate the gravitational sag.

metallized. To keep the Moliere radius small the gap for the sensors is 1 mm. The pads are contacted using an appropriate Kapton PCB and thin copper strips lead the signals to the FE electronics positioned at the outer radius of the calorimeter.

The sensors of BeamCal are similarly structured. However, due to the required higher radiation tolerance, GaAs sensors are foreseen. For the innermost part of the calorimeter, adjacent to the beam-pipe, also CVD diamond is considered.

2.3 LumiCal Simulation Studies

The cross section of Bhabha scattering can be calculated precisely from theory. In leading order it reads:

$$\frac{d\sigma_{\mathrm{B}}}{d\theta} = \frac{2\pi\alpha_{em}^2}{s}\frac{\sin\theta}{\sin^4(\theta/2)} \approx \frac{32\pi\alpha_{em}^2}{s}\frac{1}{\theta^3}, \tag{2.1}$$

where θ is the polar angle of the scattered electron with respect to the beam.

Counting the number of Bhabha events, N_{B}, in a certain θ-range, the luminosity, $\mathscr{L}$, is obtained as:

$$\mathscr{L} = \frac{N_{\mathrm{B}}}{\sigma_{\mathrm{B}}}, \tag{2.2}$$

Because of the steep θ dependence of the cross section, as illustrated in Figure 4(a), the most critical quantity to control when counting Bhabha events is the inner acceptance radius of the calorimeter, defined as the lower cut in the polar angle. Hence we need a very precise θ measurement. Furthermore, the θ-range must be chosen such that the amount of Bhabha events inside ensures the necessary statistical uncertainty. Covering a polar angle range between 40 and 60 mrad the latter requirement can be easily reached, as illustrated in Figure 4(b).

Electromagnetic showers are simulated in LumiCal using the GEANT4 [4] based package Mokka [5]. The depositions on each sensor pad are recorded, and a reconstruction of the shower is performed. The polar angle of an EM shower in LumiCal is reconstructed by performing a weighted average over the individual pads in the detector. The weight, $\mathscr{W}_i$, of a given detector

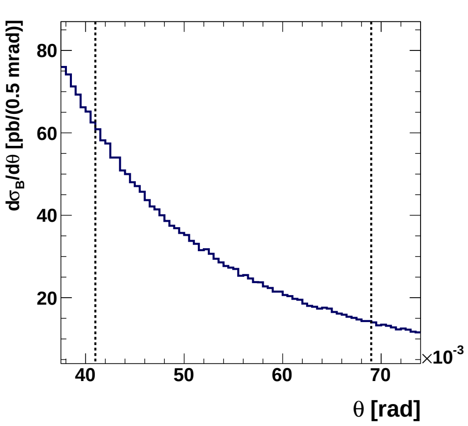

(a)

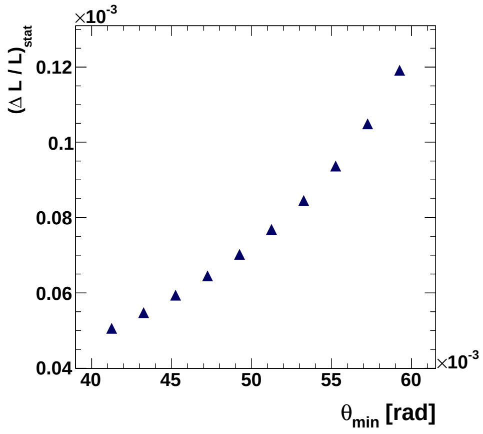

(b)

Figure 4. (a) Dependence of $d\sigma_{\mathrm{B}}/d\theta$, the differential Bhabha cross-section, on the polar angle, θ, at $\sqrt{s} = 500$ GeV. The dashed lines mark the fiducial volume of LumiCal, $41 < \theta^f < 69$ mrad. (b) Dependence of the statistical uncertainty in counting the number of Bhabha events, $(\Delta\mathscr{L}/\mathscr{L})_{stat}$, on the minimal polar angle, θ_{min}, which defines the lower edge of the fiducial volume in each case.

pad i is determined by logarithmic weighting [6], for which $\mathscr{W}_i = \max\{\, 0\ ,\ \mathscr{C} + \ln(E_i/E_{tot}\,)\}$. The symbol E_i refers to the individual pad energy, E_{tot} is the total energy in all pads, and $\mathscr{C}$ is a constant. In this way, an effective cutoff is introduced on individual hits, and only pads which contain a high percentage of the shower energy contribute to the reconstruction. The polar angle resolution, σ_θ, and the polar angle measurement bias, $\Delta\theta$, are defined as the Gaussian width and the most probable value of the distribution of the difference between the reconstructed and the generated polar angles. The existence of $\Delta\theta$ is due to the non-linear transformation between the global coordinate system of the detector, and the coordinate system of LumiCal, in which the shower position is reconstructed. There is an optimal value for $\mathscr{C}$, for which σ_θ is minimal [7, 8]. Using this optimal value for a polar angle segmentation of $\ell_\theta = 0.8$ mrad, the polar angle resolution and bias of LumiCal are $\sigma_\theta = (2.2 \pm 0.01) \cdot 10^{-2}$ and $\Delta\theta = (3.2 \pm 0.1) \cdot 10^{-3}$ mrad, respectively. The polar bias causes a shift in the luminosity measurement, since events may be pushed in or out of the fiducial volume. This shift is expressed as

$$\left(\frac{\Delta\mathscr{L}}{\mathscr{L}}\right)_{rec} \approx 2\frac{\Delta\theta}{\theta^f_{min}}\,. \tag{2.3}$$

Eqn. 2.3 implies that $\Delta\theta$ and θ^f_{min} are the two most important parameters that determine the shift in the luminosity measurement. The bias in the polar angle measurement depends on the polar angle pad size. As the granularity in the polar angle is made finer, both the angular resolution and the angular bias become smaller. Figure 5(a) shows the relative shift in the luminosity as a function of the angular pad size, ℓ_θ. For $\ell_\theta < 2$ mrad the shift in the luminosity measurement is smaller than 10^{-3}. Specifically, for the baseline value, $\ell_\theta = 0.8$ mrad, which corresponds to 64 radial divisions, the relative shift in luminosity is $(\Delta\mathscr{L}/\mathscr{L})_{rec} = 1.6 \cdot 10^{-4}$.

In practice it will be necessary to control the latter quantity by measuring the polar angle bias in a test-beam. Then a correction can be applied to the luminosity measurement. The uncertainty

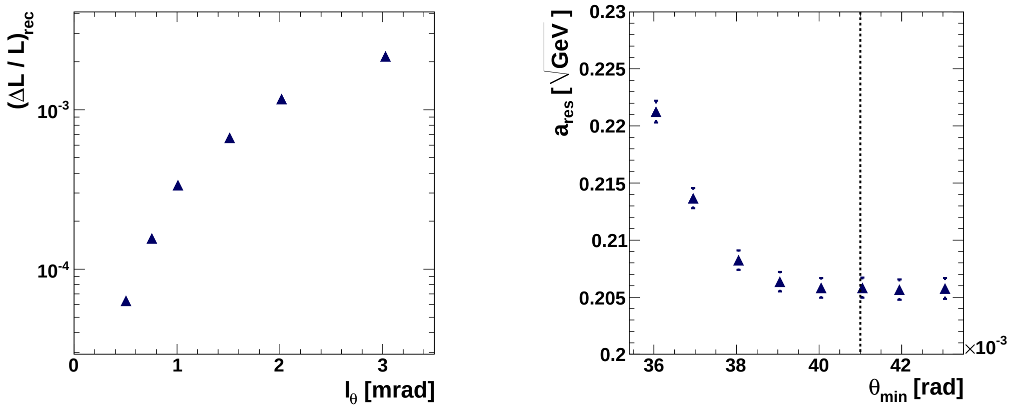

(a) (b)

Figure 5. a) Dependence of $(\Delta\mathscr{L}/\mathscr{L})_{rec}$ on the polar angle pad size, ℓ_θ. (b) The energy resolution, a_{res}, for 250 GeV electrons as a function of the polar angle, θ near the lower polar angle coverage of the calorimeter.

of the luminosity measurement is then given by the uncertainty of this quantity and may be smaller than the shift itself. The value $1.6 \cdot 10^{-4}$ is, therefore, an upper bound on the relative luminosity bias.

Using 30 radiation length tungsten as an absorber high energy electrons and photons deposit almost all of their energy in the detector. Defining fiducial cuts on the minimal and maximal reconstructed polar angles of the particles used for the luminosity measurement prevents shower leakage through the edges of LumiCal. Stable energy resolution is the hallmark of well-contained showers.

The relative energy resolution, σ_E/E, is usually parametrized as

$$\frac{\sigma_E}{E} = \frac{a_{res}}{\sqrt{E_{beam}\ (\text{GeV})}}, \tag{2.4}$$

where E and σ_E are, respectively, the most probable value, and the root-mean-square of the distribution of the energy deposited in the sensors for a beam of electrons with energy E_{beam}. Very often the parameter a_{res} is quoted as the energy resolution, a convention which will be followed here.

Figure 5(b) shows the energy resolution as a function of the polar angle θ for electron showers with energy 250 GeV. The maximal polar angle is kept constant. The best energy resolution is achieved at $\theta_{min} = 41$ mrad, where the shower is fully contained inside the calorimeter. A similar evaluation was done for a constant θ_{min} and a changing θ_{max}, resulting in an optimal cut at $\theta_{max} =$ 69 mrad. The fiducial volume of LumiCal is thus defined to be the polar angular range

$$41 < \theta^f < 69 \text{ mrad}. \tag{2.5}$$

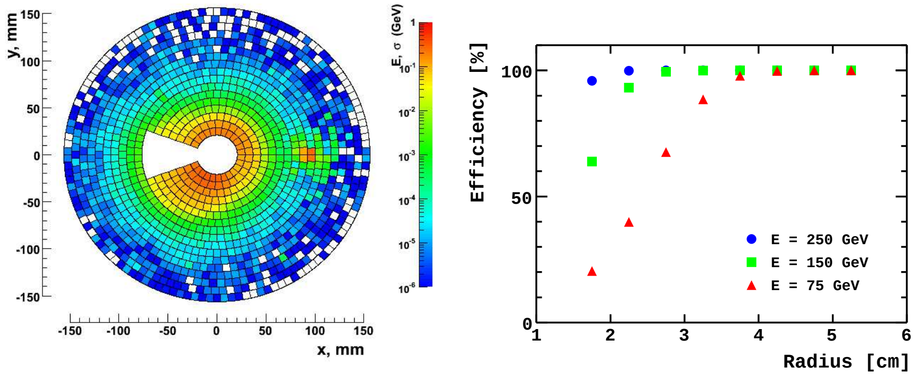

(a) (b)

Figure 6. a) The distribution of depositions of beamstrahlung pairs after one bunch crossing on BeamCal. Superimposed is the deposition of a single high energy electron (red spot at the right side). The white area in the center is foreseen for the beam-pipes. b) The efficiency to detect single high energy electrons on top of the beamstrahlung background for electron energies of 75, 150 and 250 GeV.

Using only electron showers inside the fiducial volume of LumiCal, the energy resolution is estimated to be $a_{res} = 0.21 \pm 0.02\ \sqrt{\text{GeV}}$. No dependence on the electron energy is found in the energy range from 50 to 300 GeV. In order to determine the energy of showering particles, it is necessary to know the relation between this energy and the integrated deposited energy in the detector. Here a linear dependence is found in the same energy range.

2.4 BeamCal Simulation Studies

BeamCal will be hit after each bunch-crossing by a large amount of beamstrahlung pairs. Their number, energy and spatial distribution depends on the beam parameters and the magnetic field inside the detector. Using the nominal beam-parameter set [9] beamstrahlung pairs are generated using the GUINEA-PIG program [10]. Inside the ILC detector an anti-DID field [11] is assumed, and beamstrahlung pairs are transported through the detector using a GEANT4 [4] based program.

The depositions on BeamCal per bunch crossing, up to several TeV as shown in Figure 6(a), and the shape of these depositions allow a bunch-by-bunch luminosity estimate and the determination of beam parameters with an accuracy between a few and about 10% [3].

For search experiments is is of interest to detect depositions of single high energy electrons on top of the wider spread beamstrahlung pairs. Superimposed on the pair depositions in Figure 6(a) is the local deposition of one high energy electron, seen as the red spot at the bottom. Using an appropriate subtraction of the pair deposits and a shower finding algorithm which takes into account the longitudinal shower profile, the deposition of the high energy electron can be detected with high efficiency, as shown in Figure 6(b), and modest energy resolution even at small polar angles. This feature would allow to suppress the background from two-photon processes in a search e.g. for super-symmetric tau-leptons [12] in a large fraction of the parameter space.

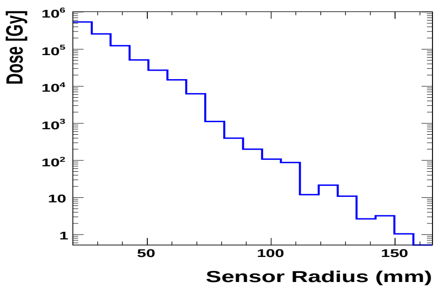

Figure 7. The dose absorbed in BeamCal sensors in MGy per year as a function of the radial distance from the beam.

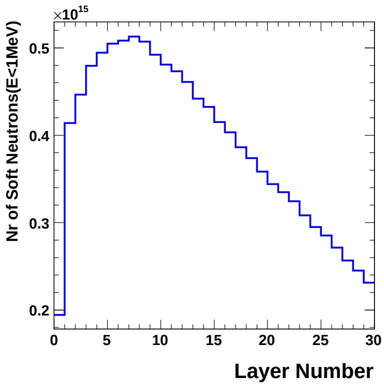

(a)

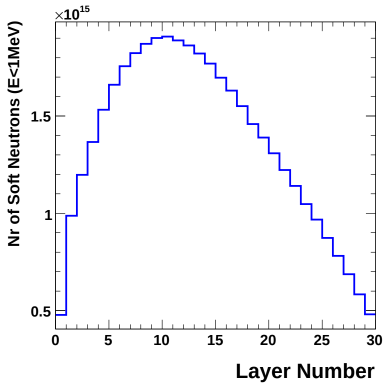

(b)

Figure 8. The flux of neutrons per year inside the sensors of BeamCal with energies below 1 MeV as a function of the sensor layer number; a) using the common Geant physics list for electromagnetic shower generation and b) using the list with the cascade model of Bertini.

The simulations are also used to determine the electromagnetic dose accumulated in the sensors and the neutron flux inside the sensors after one year of operation with nominal beam parameters. The electromagnetic dose as a function of the radius in the sensor layer with the largest depositions is shown in Figure 7 In the innermost ring of the calorimeter a dose of about 0.5 MGy is expected. Since the dose depends also on the azimuthal angle in some sensor areas of the inner rings the dose per year approaches 1 MGy.

The neutron flux is estimated using two different physics lists in Geant4. The first, the standard electromagnetic shower simulation extended by electro- and photonuclear interactions, and the second specifically designed for describing neutron interactions using the cascade model of Bertini [13]. Substantial differences, in particular in the flux of low energy neutrons, are found, as can be seen in Figures 8(a)and 8(b). The maximum of the neutron flux is by a factor of 4 larger in the second model. In addition the maximum is shifted deeper into the calorimeter and the distribution is wider. At higher neutron energies the neutron spectra of both physics lists are

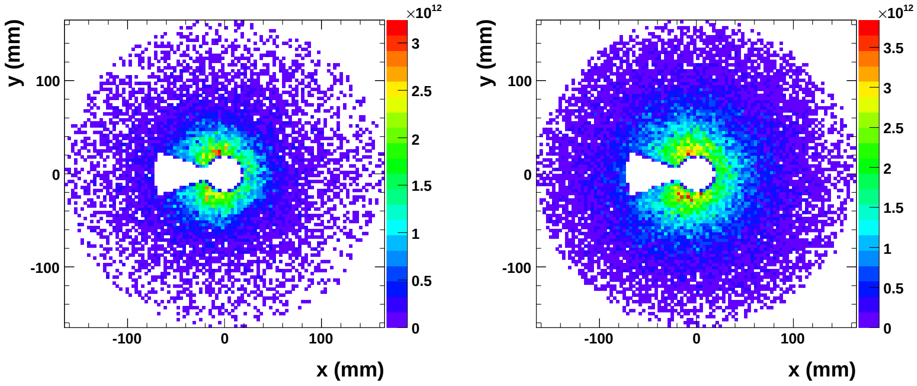

(a) (b)

Figure 9. The flux of neutrons per 3x3 mm^2 and year crossing a sensor of BeamCal with energies below 1 MeV; a) using the common Geant physics list for electromagnetic shower generation and b) using the list with the cascade model of Bertini.

comparable [14].

The radial distribution of low-energy neutrons in a sensor layer is shown in Figure 9 for one year of operation at nominal beam parameters. Using the cascade model of Bertini a neutron flux of $0.4 \cdot 10^{12}$ neutrons per mm^2 is expected near the beam-pipe.

2.5 Pair Monitor Performance

The pair monitor will consist of one layer of silicon pixel sensors just in front of BeamCal to measure the number density distribution of the number of beamstrahlung pairs. This distribution carries information on the bunch profile [15, 16]. Here we investigated the sensitivity to the horizontal and vertical bunch sizes, σ_x and σ_y, and the ratio of the vertical displacement between bunches crossing to their vertical size, Δ_y.

To reconstruct the beam profile several observables characterising the distribution of pairs at the front face of BeamCal are used [17]. Bunch crossings are simulated for a certain ranges of σ_x, σ_y, and Δ_y, and then each of these observables is fitted with a second order polynomial as a function of σ_x, σ_y, and Δ_y. Then, bunch crossings are generated using a certain set of beam parameters and σ_x, σ_y, and Δ_y are reconstructed with the inverse matrix method. Figure 10 shows the difference between the beam parameters reconstructed and set in the simulation devided by the latter, averaged over 50 bunch crossings. These quantitues are compatible with zero, and the relative uncertainties of the horizontal and vertical beam sizes and the vertical displacement are given in Table 2.5.

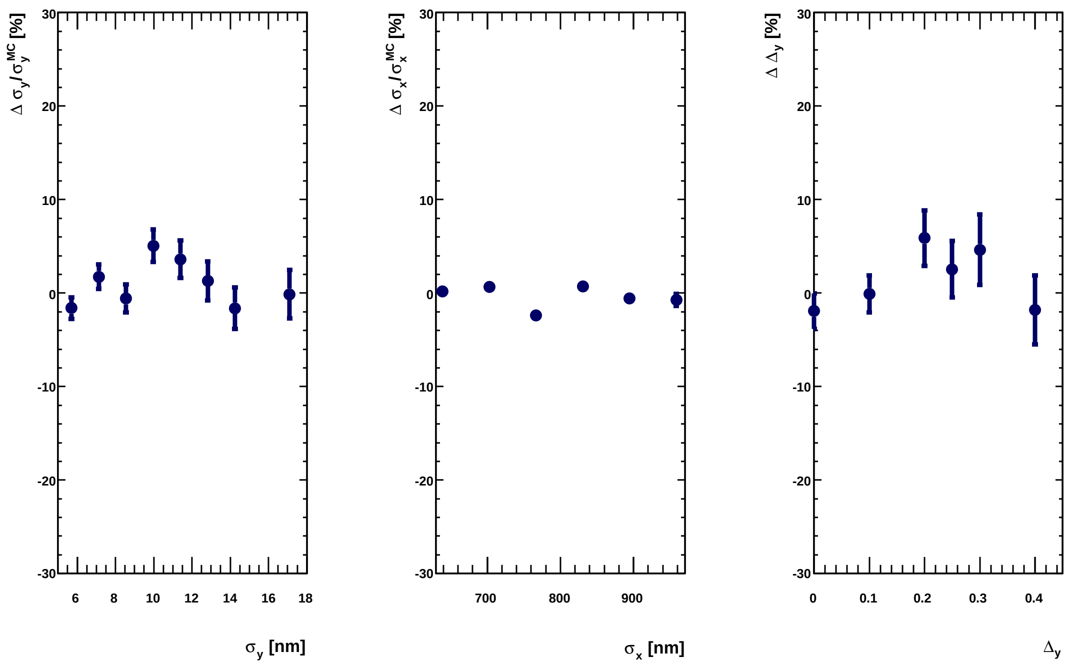

Figure 10. The relative deviations of the horizontal and vertical beam size, and ratio of vertical displacement to the vertical beam size for 50 bunch crossings which are measure by pair monitor and BeamCal.

	σ_x	σ_y	Δ_y
	3.2%	10.1%.	8.0%

Table 1. The estimated measurement accuracy of the horizontal (σ_x) and vertical beam size (σ_y), and ratio of vertical displacement to the vertical beam size (Δ_y) measured with the pair monitor.

3. Systematic Effects in the Luminosity Measurement

Several physics phenomena which may have impact on the luminosity measurement are considered here and methods how to control their impact are described. These are: the acceleration of electrons and positrons in the magnetic field when bunches are crossing, background from 2-photon processes and the resolution and scale of the electron energy measurement.

3.1 Beam-Beam Interaction

The acceleration of electrons and positrons towards the bunch center when bunches are crossing changes their momentum direction, and, more important, electrons and positrons radiate beamstrahlung prior to Bhabha scattering. The result is a reduction of Bhabha events in a given range of low polar angles [18]. This reduction is found to depend on the selection criteria for Bhabha events, and amounts for a selection based on more stringent cuts on the calorimeter on one side and more relaxed on the other to 1.51±0.05% [18] for nominal beam parameters at 500 GeV center of mass energy. The dominant contribution is due beamstrahlung reducing the centre-of-mass energy that we obtain an asymmetric beam particle energy distribution called luminosity spectrum. In the measurement of the luminosity this reduction has to be corrected for. The uncertainty, resulting from the precision to which the bunch sizes are measured and from the precison of the reconstructed luminosity spectrum, is estimated to be less than 10^{-3}.

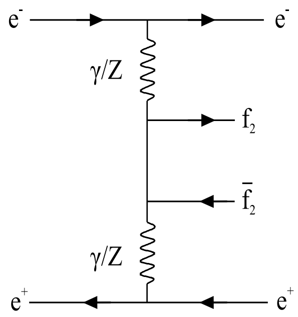

Figure 11. Dominating Feynman graph for four-fermion production.

3.2 Background From Physics Processes

Four-fermion production via neutral current exchange is known to be of large cross section with maxima at low polar angles. It is dominated by a diagram as shown in Figure 11, where two virtual photons are exchanged between electron spectators. The spectators remain at high energy. A fraction of them hits the luminosity calorimeter and manifests a background for Bhabha events. We use BDK [19] and WHIZARD [20] event generators to obtain samples of events for final states with leptons in the inner legs. The cross-sections amount to 12.0±0.5 nb and 11.7±0.4 nb at 500 GeV and 1 TeV, respectively, when the momenta of the exchanged photons are required to be larger than 0.1 GeV/c. A Bhabha sample of 5 pb^{-1} has been generated with cross-sections of (4.70±0.03) nb and (1.20±0.03) nb, for 500 GeV and 1 TeV centre-of-mass energy, respectively, using the BHLUMI [21] event generator. The detector response is simulated using BARBIE V4.3 [22], a GEANT3 based simulation program of LumiCal. The following event selection criteria are applied: the polar angles of the reconstructed shower must be within the LumiCal fiducial volume at one side and within $\theta_{min} + 4$ mrad and θ_{max} - 7 mrad) on the other side [18] and the total shower energy must be more than 80% of the center-of-mass energy. The reduction of four-fermion events in the LumiCal after application of the Bhabha selection criteria is illustrated in Figure 12 where the hits of particles from the four-fermion final states in the front plane of the luminosity calorimeter are shown. The Bhabha event selection efficiency is about 68%.

As can be seen from Table 2, the Bhabha selection criteria suppress the four-fermion events by at least factor of 10. In addition, since the fraction of events with depositions in the LumiCal and the event kinematics in the samples generated with WHIZARD and BDK are also different, the large differences in the cross sections mentioned above are almost compensated leading to very similar background to signal ratios for both Monte Carlo generators of about 2 and $2.5\cdot10^{-4}$ at 500 GeV and 3.5 and $7.4\cdot10^{-4}$ at 1 TeV centre-of-mass energy, respectively. The shift on the luminosity

		500 GeV	1 TeV
	WHIZARD	8.0	4.8
F$\cdot$ 10^{-2} [%]	BDK	2.5	1.7
	WHIZARD	17.9	19.0
Eff[%]	BDK	9.9	7.1

Table 2. The fractions F[%] of for-fermion events in LumiCal obtained from the WHIZARD and BDK event samples scaled down by a factor of 100 and the efficiency (Eff [%]) to select them after applying Bhabha selection criteria for the same samples for centre-of-mass energies of 500 GeV and 1 TeV.

		500 GeV	1 TeV
	WHIZARD	$2.3{\cdot}10^{-3}$	$1.8{\cdot}10^{-3}$
B/S before selection	BDK	$7.9{\cdot}10^{-3}$	$3.6{\cdot}10^{-2}$
	WHIZARD	$2.0{\cdot}10^{-4}$	$3.5{\cdot}10^{-4}$
B/S after selection	BDK	$2.5{\cdot}10^{-4}$	$7.4{\cdot}10^{-4}$

Table 3. The fraction of four-fermion events, denoted as background, and the background to signal (B/S) ratio, before and after Bhabha event selection, for WHIZARD and BDK at centre-of-mass energies of 500 GeV and 1 TeV, respectively.

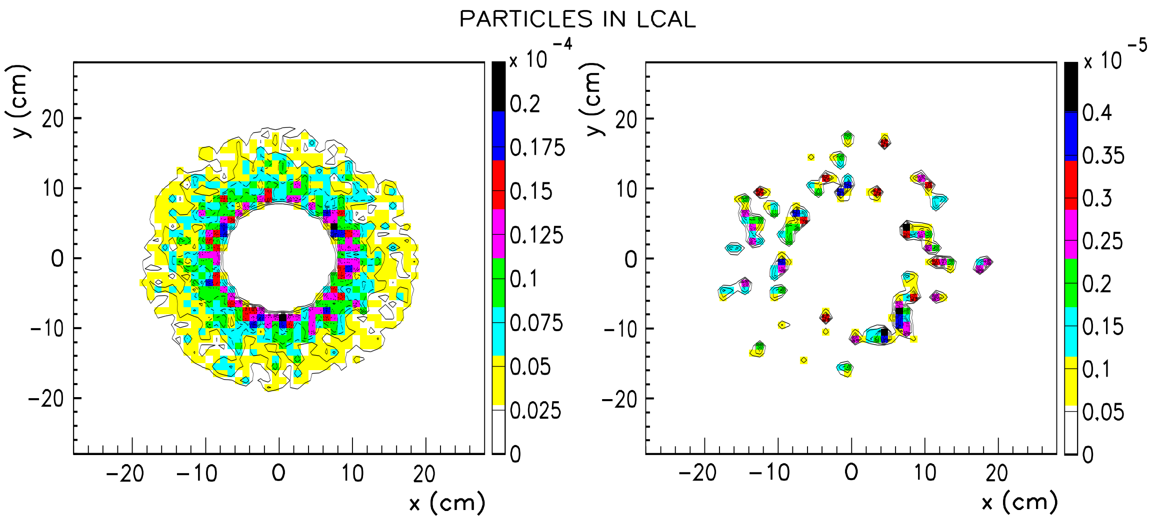

Figure 12. Projected hits originating from four-fermion interactions per bunch crossing on the first plane of the luminosity calorimeter at 500 GeV, before (left) and after (right) application of Bhabha event selection criteria.

measurement originating from four-fermion events, even if it is expected to be below the required precision of the luminosity measurement, may be applied as a correction.

3.3 Effects of a Bias in the Energy Resolution and the Energy Scale

One of the criteria to select Bhabha events is that the total energy measured in the calorimeters is larger than 80% of the centre-of-mass energy. A possible bias in the energy resolution or the energy calibration scale factor will result in a change of the number of selected Bhabha events and hence in the measured luminosity.

The selection efficiency for Bhabha events as a function of the required energy in the calorimeter is shown in Figure 13 (a). At the position of the cut in the measured calorimeter energy the slope of the tangent to the function is about $1.8 \cdot 10^{-3}$ To keep the shift of the luminosity below 10^{-4}, the cut in the measured calorimeter energy must be controlled with a precision of about 40 MeV. A similar study applying an offset to the measured energy leads to a value of 64 MeV for a shift of 10^{-4}.

The effect of a bias in the energy resolution, the parameter a_{res} in Eqn. (2.4), is illustrated in Figure 13 (b). Here the measured shower energy is smeared to simulate a worsening of the energy resolution parameter a_{res}. To keep the shift in the luminosity less than 10^{-4}, this quantity must be controlled to better than 1.5%

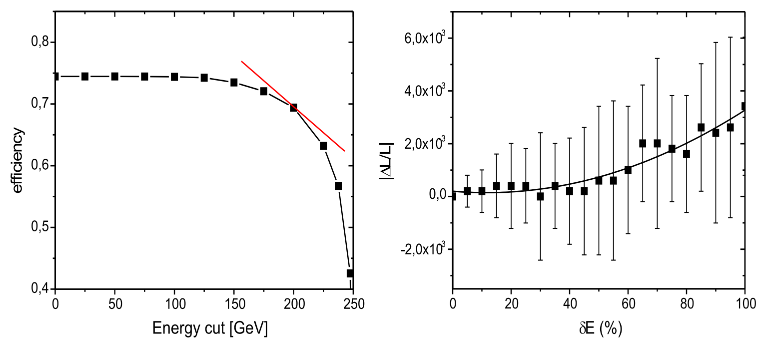

(a) (b)

Figure 13. (a) The selection efficiency for Bhabha events as a function of the measured shower energy, (b) The shift of the measured luminosity as a function of the bias in the energy resolution parameter a_{res}.

4. Sensor Development

4.1 BeamCal

The challenge of BeamCal are sensors tolerating about a MGy of dose per year. So far we have studied polycrystalline CVD diamond sensors of 1 cm^2 size, and larger sectors of GaAs pad sensors as shown in Figure 14. Irradiation studies are done using a 10 MeV electron beam at the sDALINAC accelerator [citation] varying the intensity between 10 and 100 nA corresponding to dose rates of 10 to 200 kGy/h. Polycrystalline CVD diamond sensors are irradiated up to 7 MGy and are still operational [23]. In a first study GaAs sensors are found to tolerate about 1.5 MGy

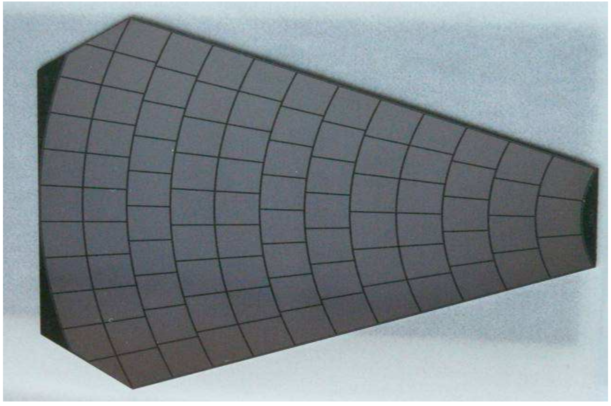

Figure 14. A prototype of a GaAs sensor sector for BeamCal with pads of about 0.3 cm^2 area.

[24]. Since large area CVD diamond sensors are extremely expensive, they may be used only at the innermost part of BeamCal. At larger radii GaAs sensors seem to be a promising option.

4.1.1 GaAs

Large area GaAs sensors are obtained from the Siberian Institute of Technology. They are produced in liquid encapsulated Czochralski method and doped with thin and tellur as shallow donors and chromium as deep acceptor.

Three batches with different concentrations of dopants are irradiated up to 1.2 MGy and the charge collection efficiency is measured as a function of the absorbed dose. For all sensors a MIP signal is separated from the pedestal up to a dose of 600 kGy. The charge collection efficiency depends slightly on the dopant concentration. The sensors with a lower donor concentration show a larger initial charge collection efficiency and the decrease of the charge collection efficiency as a function of the absorbed dose is less steep, as can be seen in Figure 15.

4.1.2 scCVD Diamond

A single crystal CVD diamond sensor has been irradiated in two steps up to 10 MGy. The dependence of CCD on the absorbed dose is shown in the Figure 16. Blue sqares correspond to the first and red dots to the second test-beam irradiation. It is clearly seen that no annealing of the damaged crystal during almost 1.5 years is observed. We have studied in more detail the mechanism of the charge collection in the radiation damaged diamond sensor. It was found that in the damaged detector, operating under bias voltage, strong polarization develops in the bulk of the sensor material [**?**]. This polarization, together with trapping of the charge carriers, is responsible for the drop of charge collection efficiency. Regular change of the bias voltage polarity eliminates the polarization and speeds up the filling of long-living traps (*pumping* or *priming* effect). This way a significant part of efficiency can be recovered. It can be seen for example in the Figure 16a), where time evolution of the signal from the 10 MGy damaged detector is presented for different operating conditions. The red dots show the slow development of polarization when a constant high voltage is applied reducing the charge collection efficiency to a few per cent. The other measurements shown in Figure 16b) demonstrate the recovery of charg collection efficiency at different operating conditions with alternating high voltage polarity.

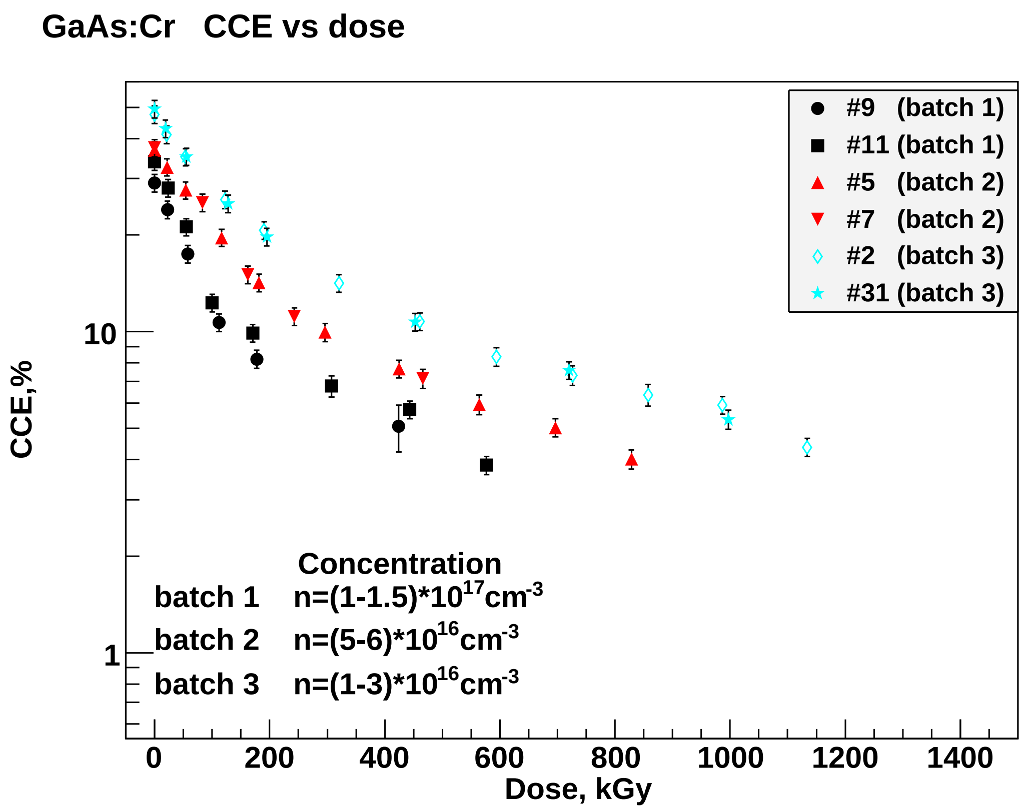

Figure 15. The CCE as a function of the absorbed dose for the GaAs sensors with different donor concentrations. The donor impurity is Te for the batches 1 and 2 and Sn for batch 3.

4.2 Sensors for LumiCal

Prototypes of LumiCal sensors have been produced by Hamamatsu Photonics. A picture of a sensor is shown in Figure 17. By shape it is a ring segment of 30°. The thickness of the n-type silicon bulk is 320 μm. The pitch of the concentric p^+ strips is 1.8 mm and the gap between two strips is 0.1 mm. In Figure **??** the leakage currents of several pads of one sensor at a bias voltage of 500 V are shown . All pads except one have a leakage current in the range from 1 to 4 nA. Less than 5% of all pads have a break-through voltage below 500 V. For the other sensors the results are similar. The influence of grounded neighbor pads on the leakage current measurement can be seen in Figure 18. The leakage current is reduced and kept constant when the sensor is fully depleted. The measured leakage currents are between 1 and 2 nA for this case. The C/V curves for several pads are shown in Figure 19 (a). The capacitances are proportional to the pad size. At a voltage of 150 V the pad capacitance values are 25 pF for the largest pads and 10 pF for the smallest pads, respectively. In Figure 19(b) it is shown how the value of the full depletion voltage is obtained. Values from 39 V to 43 V were found.

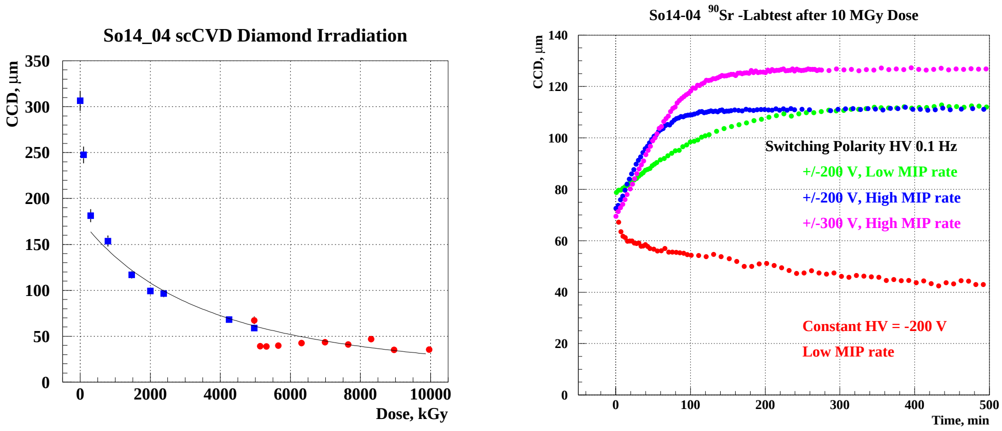

(a) (b)

Figure 16. (a) The CCD of a diamond sensor as a function of the absorbed dose. The blue squares are measured in 2007 and the red dots in a second irradiation in 2009, (b) Charge collection efficiency as a function of time for an irradiated diamond sensor operated with constant are polarity changing high voltage.

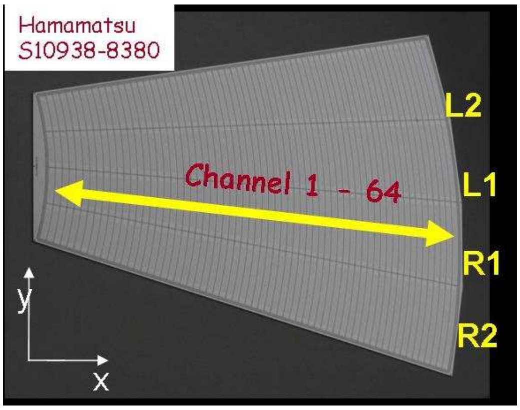

Figure 17. A prototype silicon sensor for LumiCal

5. ASIC Developments

5.1 LumiCal Readout

The design of the LumiCal front–end electronics depends on several assumptions and requirements concerning detector architecture [27]. The front–end should work in two modes: the physics mode and the calibration mode. In the physics mode the detector should be sensitive to electromagnetic showers resulting in high energy deposition and the front–end should process signals up to 10 pC or even more per channel. In the calibration mode it should detect signals from relativistic muons, i.e. should be able to register the minimum ionising particles (MIPs). Then signals as small as 2 fC, corresponding to low end of the Landau distribution for MIPs in 300 μm thick silicon, should be detected. The proposed sensor geometry results in very wide range 10 pF – 100 pF of strip ca-

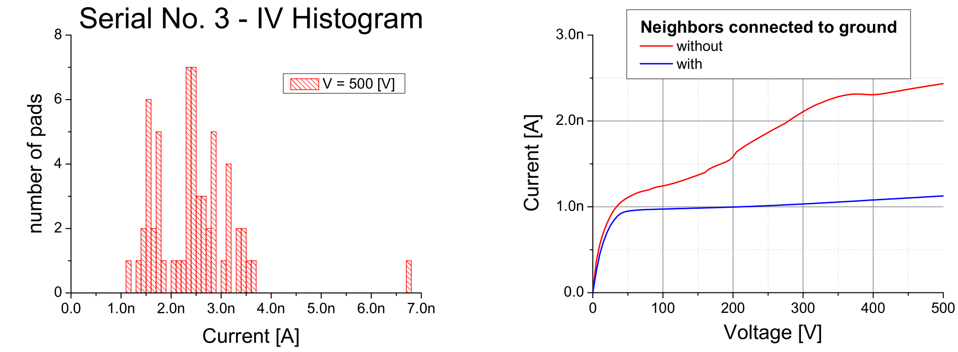

(a) (b)

Figure 18. IV curve for a single pad with and without connected neighbors. Measured dark currents for a selected sensor

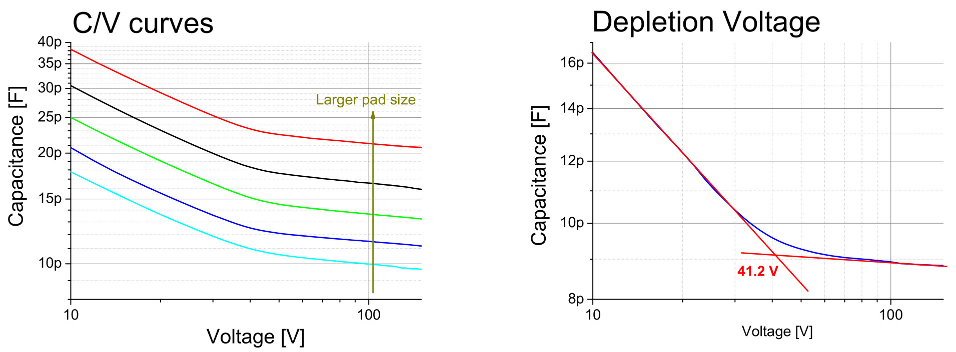

(a) (b)

Figure 19. Measured CV-curves and depletion voltage for a sensor prototype.

pacitance connected to a single front–end channel. Because of very high expected strip occupancy, the front–end should be fast enough to resolve signals from subsequent beam bunches which are separated in time by about 300 ns.

The simulations of LumiCal indicate that the shower reconstruction needs about 10 bit precision. Severe requirements are set on the readout electronics power dissipation may be strongly relaxed if switching of the power between bunch trains is implemented. This is feasible since in the ILC experiments after each 1 ms bunch train there will be about 200 ms pause [26].

To fulfil the above specifications the general concept of the full readout chain comprising a front-end electronics, a digitiser (ADC) plus zero suppression and a data concentrator with optical driver is chosen. One ADC may serve for one or for more channels. In the following the design and the measurements of prototype front–end and the ADC ASICs are presented. The prototype ASICs are fabricated in 0.35 μm CMOS technology. A more detailed discussions of the front–end may be found in [28] and of the ADC in [29]. The data concentrator is not designed yet but since its first prototype is expected to be developed using the FPGA circuits, the development time should be significantly shorter than the rest of the readout chain.

5.1.1 Front–end Electronics Design

The chosen front–end architecture comprises a charge sensitive amplifier, a pole–zero cancellation circuit (PZC) and a shaper, as shown in Figure 20. In order to cope with large charges in the physics mode and the small ones in the calibration mode a variable gain in both the charge amplifier and the shaper is applied. The "mode" switch in Figure 20 changes effective values of the feedback circuit components R_f, C_f, R_i, C_i and so changes the transimpedance gain of the front–end. The

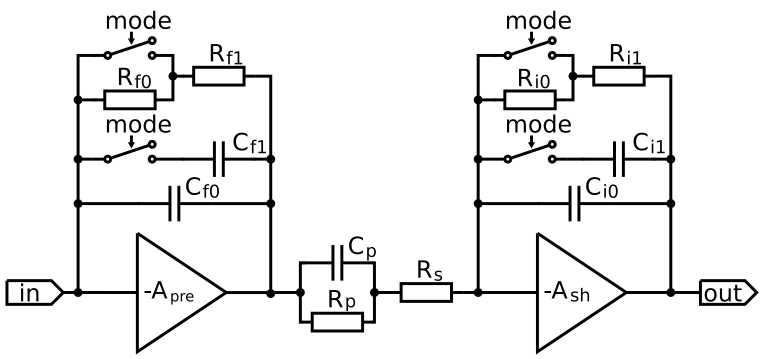

Figure 20. Block diagram of the single front–end channel

low gain (large C_f) is used for the physics mode when the front–end processes signals from large charge depositions in the sensor, while the high gain (small C_f) is used in the calibration mode when a MIP sensitivity is needed. The same concerns the terms calibration mode and high gain mode. Assuming high enough open loop gain of the preamplifier (A_{pre}) and the shaper amplifier (A_{sh}), the transfer function of this circuit is given as:

$$\frac{U_{out}(s)}{I_{in}(s)} = \frac{1}{C_f C_i R_s} \cdot \frac{s + 1/C_p R_p}{s + 1/C_f R_f} \cdot \frac{1}{(s + 1/C_i R_i)(s + 1/C_p(R_p||R_s))}. \tag{5.1}$$

Setting properly the PZC parameters ($C_f R_f = C_p R_p$) and equalising shaping time constants ($C_i R_i = C_p(R_p||R_s)$) one obtains the first order shaping, equivalent to a CR–RC filter, with a peaking time $T_{peak} = C_i R_i$. A simple first order shaping is chosen as a tradeoff between the noise and the power dissipation. Regarding the noise a main requirement is to obtain in calibration mode the signal to noise ratio (S/N) of about 10 for the largest sensor capacitances. Both of the amplifying stages (A_{pre}, A_{sh}) are designed as the folded cascodes [30] with active loads, followed by the source followers. In the prototype ASIC 8 front–end channels are implemented. Four channels are designed with passive feedback and PZC resistances R_f, R_p while the other four channels use MOS transistors in a triode region to this aim [31]. This allows us to compare overall performances of the two feedback schemes.

5.1.2 Front–end Electronics Measurements

The photograph of prototype ASIC glued and bonded on the PCB is shown Figure 21. The power

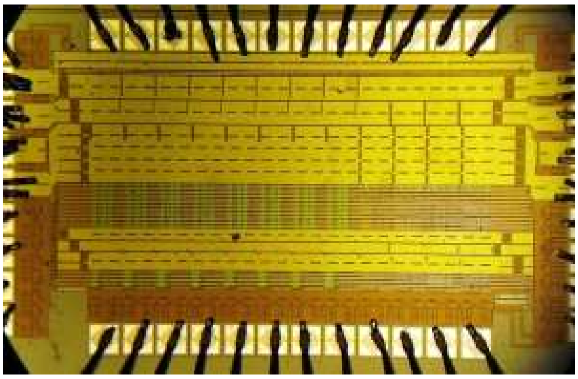

Figure 21. Photograph of glued and bonded FE prototype

consumption of about 8.9 mW/channel is measured what confirms well the simulations.

Figure 22 shows the response of the front–end channel to charge injected through the input test capacitance for different values of input capacitance (C_{det}) within the interesting range. The sensor capacitance is simulated with an external capacitor. For the physics mode the results obtained

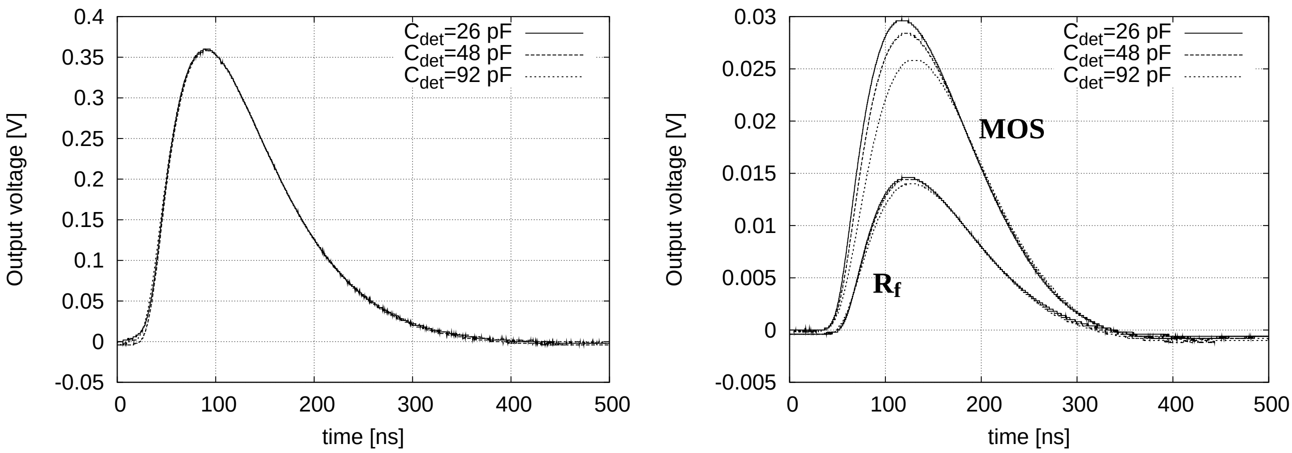

Figure 22. Output pulses for MOS resistor front–end channels in physics mode (left) and for MOS and R_f resistor in calibration mode (right), as a function of input capacitance. In calibration mode $Q_{in} = 10\ fC$, while in physics mode $Q_{in} = 3.3\ pC$

for active (MOS) and passive (R_f) feedback are exactly the same and so only the active feedback curves are shown in the plot. It is seen that both, the amplitude and the peaking time ($\sim$70 ns), are not sensitive to the value of the input capacitance in this case. In the calibration mode the amplitude and the peaking time depend on the input capacitance (C_{det}). The described measurements are in good agreement with Hspice simulations performed for both types of feedback resistors and both gain modes.

The output noise has been measured using a HP3400 true rms meter. The equivalent noise charge (ENC) as a function of input capacitance is shown in Figure. 23. Similar results are obtained for active and passive feedback. Results obtained for the physics and calibration modes are shown on the same plots. Since the HP3400 bandwidth is only up to 10 MHz the numbers

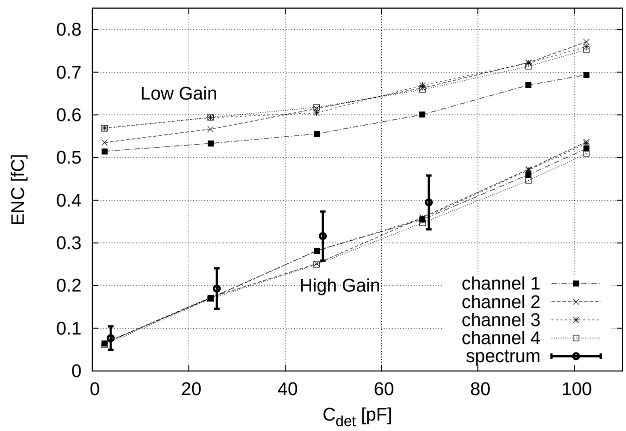

Figure 23. Noise ENC measurements obtained with true rms meter for the front–end with passive feedback

may by underestimated by about 20%. The ENC vs C_{det} behaviour and the measured values are generally in agreement with simulations. In particular, in the calibration mode the signal to noise ratio of 10 is maintained for input capacitances up to about 100 pF. For a few points additional noise measurements have been performed by measuring the output noise spectra using a HP4195A spectrum analyser and then integrating it numerically. The results of such measurements are added in Figure 23. They agree within their uncertainties with the HP3400 measurements.

In order to test the effectiveness of the PZC circuit the front–end response has been measured as a function of the rate of input pulses. To avoid input charges of both polarities when using a square–wave test signal, the staircase test waveforms are synthesised using the Tektronix AWG2021 waveform generator. It was found that the change in amplitude reaches 2% for input rates of about 3 MHz and is almost not sensitive to the input capacitance.

5.1.3 ADC design

As a compromise between speed, area and power consumption the ADC was designd in the pipeline technology. A 1.5-bit per stage architecture is chosen because of its simplicity and immunity to the offsets in the comparator and amplifier circuits. The block diagram of a single stage is shown in Figure 24. Each 1.5-bit stage consist of two comparators, two pairs of capacitors C_s and C_f, an operational transconductance amplifier, several switches and small digital logic circuit. To improve the ADC immunity to digital crosstalks and other disturbances a fully differential architecture is used.

Two ADC prototypes were designed and produced. In the first one only the ADC core i.e. the eight 1.5-bit stages were implemented. The performed measurements showed that the prototype was fully functional although some of the measured parameters needed to be improved [29]. In the second prototype a complete ADC comprising the input sample and hold (S/H) circuit, 9 pipeline stages, digital correction circuitry and the power switching feature are implemented. In the following results of performance measurements of this new prototype are briefly discussed.

5.1.4 ADC performance measurements

The photograph of the ADC prototype is shown Figure 25. The static measurements of the Integral

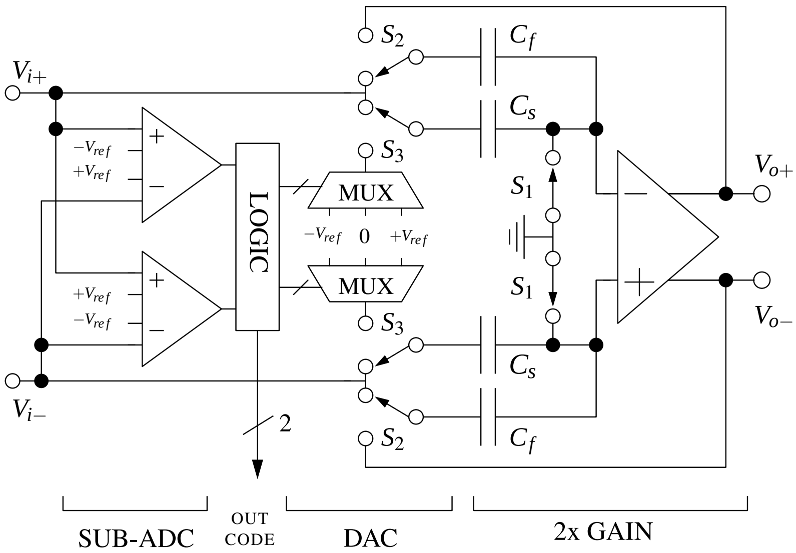

Figure 24. Simplified schematic of a 1.5-bit stage

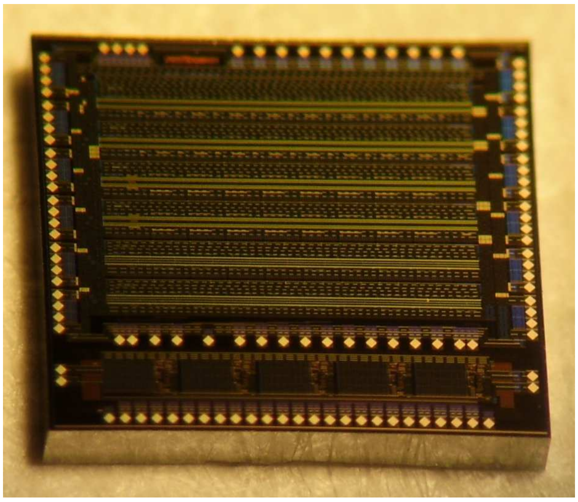

Figure 25. Photograph of ADC prototype

Nonlinearity (INL) and the Differential Nonlinearity (DNL), obtained at a sampling frequency of 20 MHz, are shown in Figure 26. These parameters are calculated using the histogramming method. The measured INL is always less than 1 LSB while the DNL is below 0.5 LSB. These results attest to very good ADC linearity.

To estimate the dynamic performance measurements with pure sinusoidal wave input are performed [32]. An example of a measured spectrum using a 1.8 MHz full scale (0 dB) input signal sampled at 20 MHz is shown in Figure 27. It is seen that the noise and harmonic components are small enough not affecting significantly the resolution. The signal to noise ratio (SNHR) is measured as a function of sampling frequency as shown in Figure 28. An SNHR of about 58 dB is obtained in the frequency range up to almost 25 MHz.

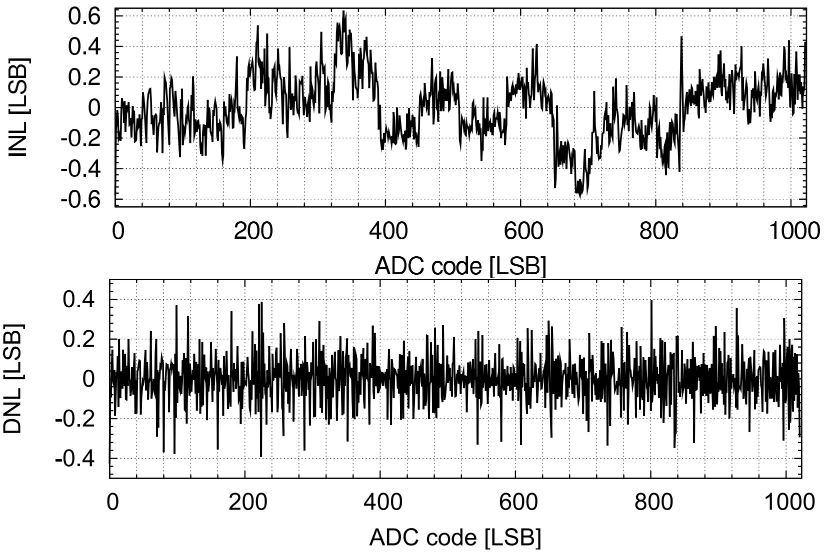

Figure 26. Static measurements of INL and DNL errors

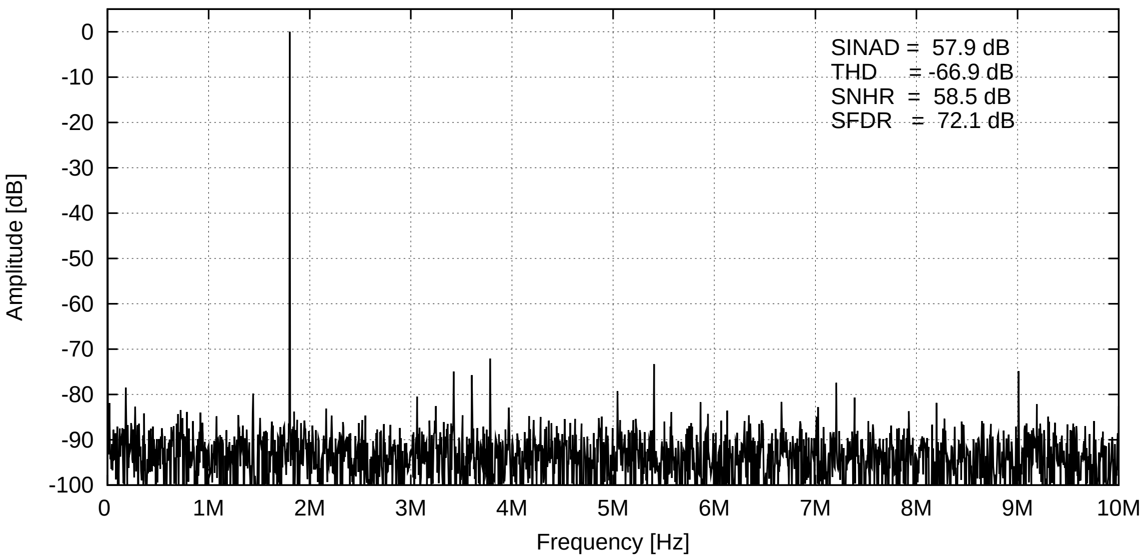

Figure 27. Example of FFT measurement with f_{in}=1.8 MHz and f_{clk}=20 MHz

5.2 BeamCal Readout

The BeamCal ASIC, designed for 180-nanometer TSMC technology, will be able to handle 32 channels. The two modes of operation require a FE circuit capable of a wide performance envelope: high slew rate for standard data taking, and low noise for calibration operation. In standard data taking the occupancy is high, and therefore all data from a bunch train must be recorded, to be read out between bunch trains. Because of its reliability, density and redundancy possibilities, a digital memory array will be used to store the data from all collisions in each bunch train. This choice requires a sampling rate of 3.25MHz per channel, which is achieved by 10-bits, successive approximation analog-to-digital converters [33]. The small size of this ADC architecture allows to

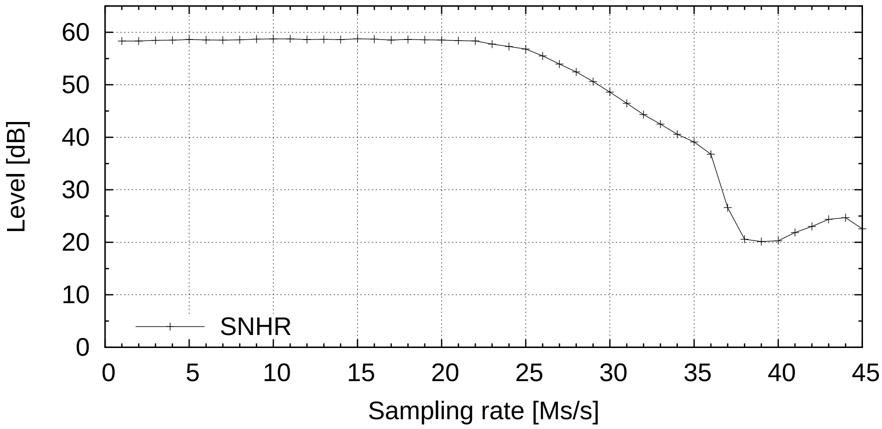

Figure 28. ADC performance as a function of sampling rate

use one converter per channel.

In this front-end, the dominant noise source is the series noise of the charge sensitive amplifier. The 40-pF input capacitance, the high occupancy and the 308-ns period make it necessary a careful design of noise filtering and baseline restoration [34].

In order to take advantage of sufficient time available for signal processing, the filter for calibration operation has been implemented using switched-capacitor (SC) circuits [35]. This technique allows to precisely define the circuit time constants depending on the input clock frequency and the ratio of two capacitors. Baseline restoration is achieved by means of a fast gated reset, followed by a slow reset-release technique to reduce the effect of a split doublet. The slow reset-release is implemented using SC circuits.

The required slew rate in standard data taking operation is achieved by a folded cascode charge-sensitive amplifier. In this mode of operation, an adequate noise power is effectively achieved by means of a slow reset-release technique, similar to that used in calibration operation. An explicit filter for standard data taking operation is unnecessary, as the CSA bandwidth suffices for noise filtering purposes.

Figure 29 shows a simplified block diagram for a single channel. In standard data taking operation, since the integrator is unnecessary for filtering, it is bypassed to reduce power consumption.

For design purposes, the transistor-level noise analysis has been carried out using the g_m/I_D technique [36], which takes noise coefficients directly from SPICE simulation results. As this is a gated front-end, the system-level noise analysis has been done using the weighting function approach.

Since the system's dominant noise source is series noise, a triangular-shaped weighting function effectively minimizes the output noise power. The negative slope section of the triangular weighting function is easily implemented by means of an integrator – in this case, a SC integrator. The positive slope section is achieved by means of the slow reset-release technique mentioned earlier. The weighting function resulting from an ideal reset-release and a SC integrator is shown in figure 30; a more realistic weighting function, reconstructed from SPICE simulation results, is shown in figure 31. In both cases, the target noise level is effectively achieved.

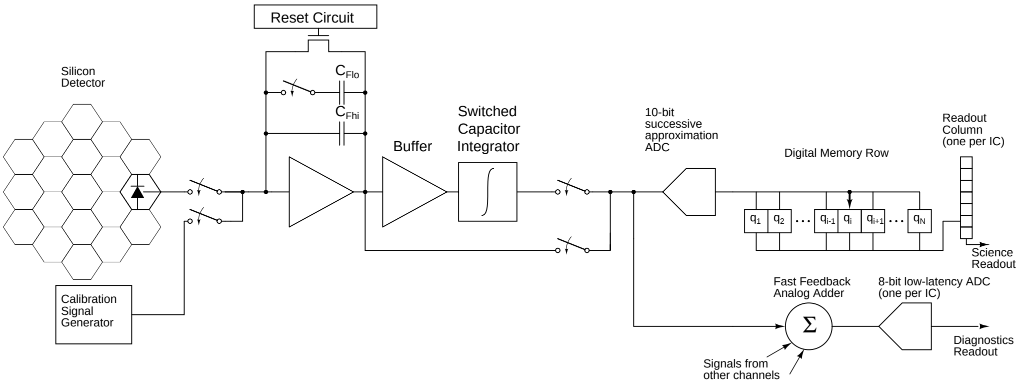

Figure 29. Simplified BeamCal ASIC block diagram, single channel

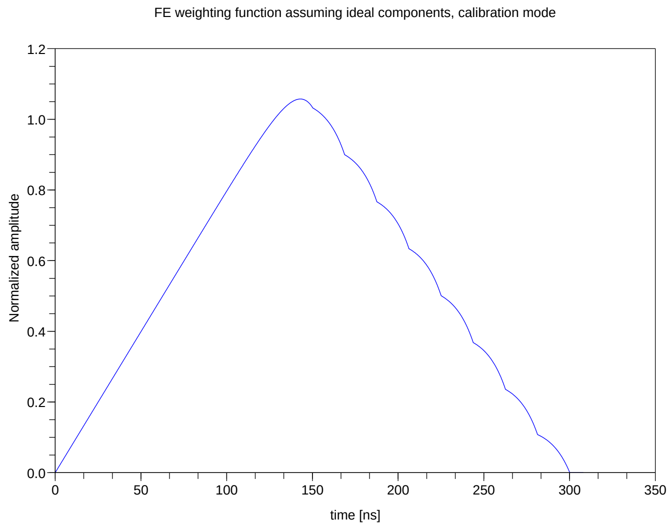

Figure 30. FE weighting function assuming ideal components, calibration mode

5.2.1 Circuit Implementation

The CSA is the folded-cascode, NMOS-based amplifier shown in figure 32, connected to the feedback network shown in figure 33. The CSA input transistor is biased at 450 μA, whereas the load works at about 50 μA. The feedback network consist of two feedback capacitors of 0.9 pF and 44.1 pF for calibration and standard data taking modes, correspondingly. Both have a reset transistor, with V_G driven by the SC reset-release network. The CSA output is pseudo-differential.

In order to isolate the CSA from the filter's SC-related kickback noise, a buffer circuit is used. The buffer also allows signal shifting, driven by a SC network, which produces a more adequate common-mode (CM) level for the filter. The buffer consumes 130μA and consists of a source follower, with cascoded current source and an additional device to keep a nearly constant V_{DS} in the input transistor. These measures enhance the buffer linearity. The buffer schematic is shown in figure 34.

The filter implemented is the SC integrator shown in figure 35. Capacitor values were carfully

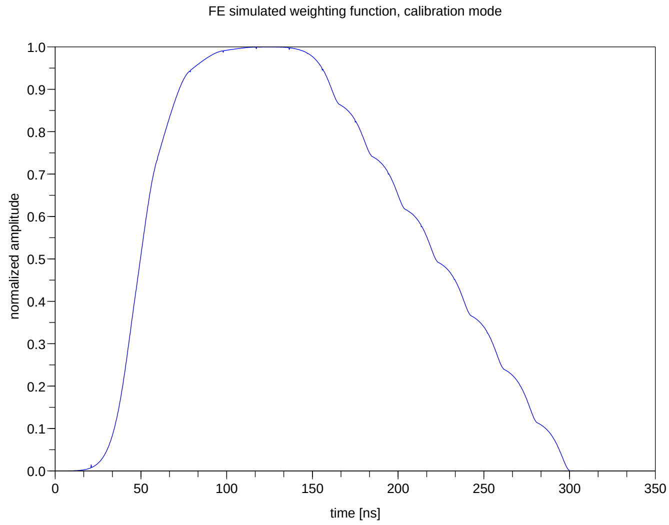

Figure 31. FE simulated weighting function (SPICE), calibration mode

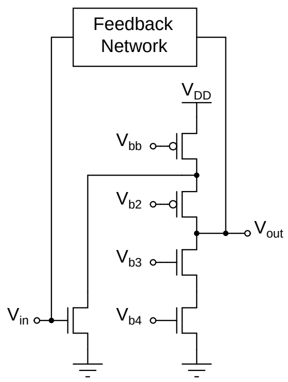

Figure 32. Charge-sensitive amplifier (CSA) simplified schematic

designed in order to obtain the adequate noise performance. The core of the integrator is the class A/AB amplifier shown in figure 36 [37]. The first stage is biased at 56μA, and the second stage consumes nearly 400μA, quiescent current. As the second stage current is set by the first stage output CM voltage, two independent CM feedback networks are required, one per stage. Both are effectively implemented as SC networks.

The ADC has been fabricated in TSMC025 and first test results for INL and DNL are promising.

5.2.2 FE simulation results

The circuit has been extensively simulated to ensure a proper performance in terms of linearity, speed and noise. Figure 37 shows typical CSA output waveforms for different input charges, whereas figure 38 presents the corresponding filter output waveforms.

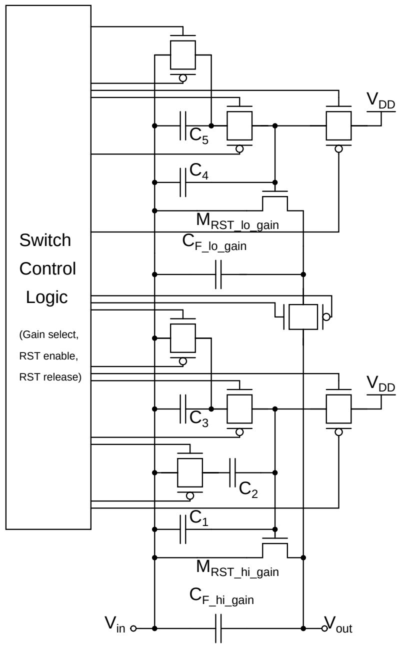

Figure 33. CSA feedback network simplified schematic

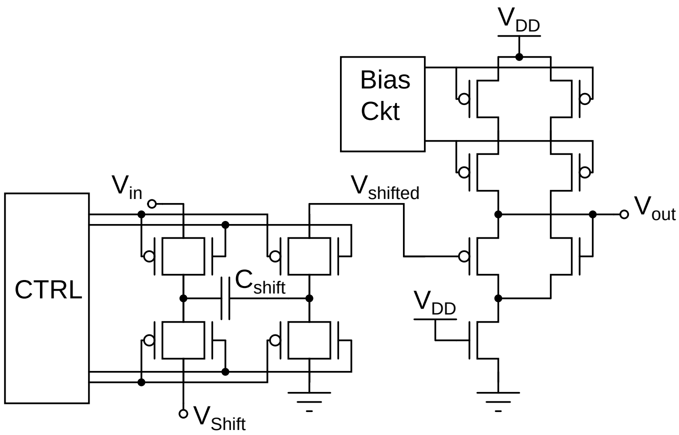

Figure 34. FE buffer schematic

5.3 Pair Monitor

We designed the prototype ASIC to have 36 readout cells arranged as an array of 6 x 6 as shown in Figure 39. Each cell has an amplifier block, comparator, 8-bit counter and 16 count-registers. The amplifier block consists of charge sensitive pre-amplifier, threshold block and differential-amplifier. The pre-amplifier is a constant-current feedback-type amplifier. The time-over-threshold (TOT) of the output signal is proportional to the injected charge through the constant current feedback in the pre-amplifier. In the 8-bit counter, the gray code is used to count the number of hits. The 16 count-registers are prepared to store hit counts at each 16 parts in one beam train. There are also decoders which select a count-register to store and readout the hit count. A shift register to select a readout

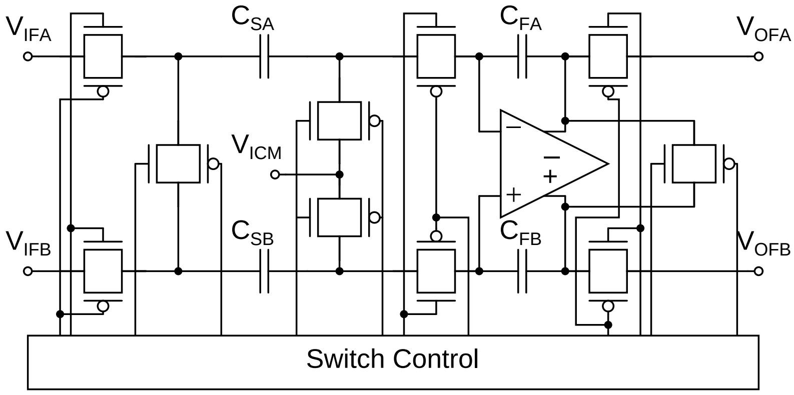

Figure 35. Switched-capacitor integrator simplified schematic

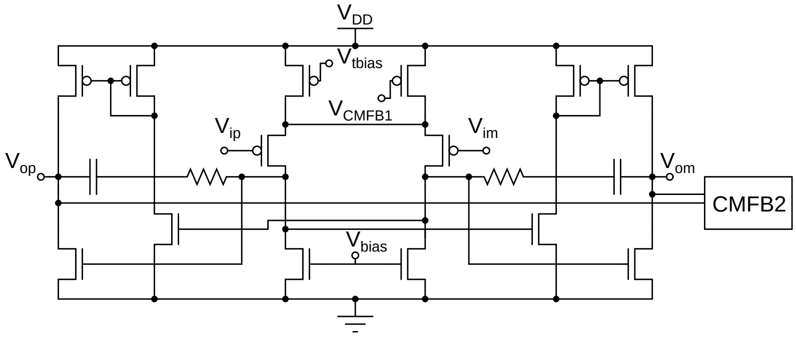

Figure 36. Filter fully differential amplifier simplified schematic

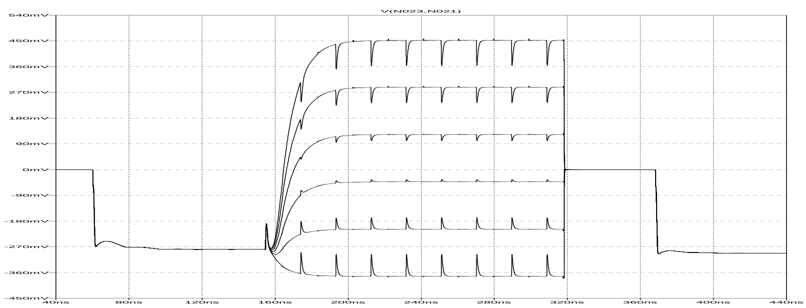

Figure 37. CSA output waveforms for different input signals

pixel, data transfer to the output line and distributor of the operation signals are arranged around the 36 readout cells as a glue logic. The bonding pad is prepared in each cell to be attached to a sensor with bump bonding. The prototype ASIC has been produced with TSMC 0.25-μm CMOS process. The chip size is 4×4 mm^2, and the readout cell size is 400 × 400 μm^2. The chip was packaged in PGA144 for the operation tests.

Figure 40(a) shows the response of the counter block. The state of the counter bits can be seen to change at the timing of the test pulse. The pair monitor measures the hit counts for 16 time slices in one train, switching over the 16 count-registers. The stored data is then read out during the

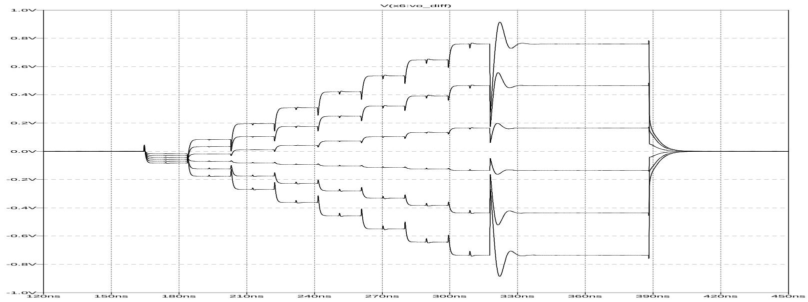

Figure 38. Full front-end output waveforms for different input signals

Figure 39. Picture of the prototype of the readout ASIC and schematic diagram of the circuit in a readout cell. The readout cell consists of the amplifier, comparator, 8-bit counter, and 16 count-registers.

inter-train gap. The test was thus performed with the same procedure as above with the hit count in each time slice changed from 0 to 255. In the pair monitor, the estimated count rate within train is below 2.5 MHz per one pixel, which corresponds to less than one hit per one bunch crossing. For that reason, the count rate is set to 4 MHz which meets the requirement. Input and output counts for one count-register are shown in Fig. 40(b). The number of hits was counted without any bit lost.

We studied the noise level in the circuit. The count efficiency was investigated as a function of the threshold voltage at the comparator. Fitting the efficiency curve with the error function, a standard deviation of 0.94 mV was obtained. With the gain of 1.6×10^{-3} mV/e, it corresponds to the equivalent noise charge (ENC) of about 600 electrons. The noise level estimated by SPICE simulation is about 100 electrons, and thus the main component of the noise seems to come from the test system. This noise level, however, is still much smaller than the typical signal level of 20,000 electrons.

Figure 40. (a) Output signals from the counter block. Q1, Q2, and Q3 show the lower 3 bit of the 8-bit counter. The Gray code is used to count the number of hits. (b) The relation between a number of the readout count from one of the count-registers (N_{OUT}) and that of the input test pulse (N_{IN}). The count rate is set to 4 MHz.

For the next step, we plan to develop the pair-monitor with SOI (Silicon On Insulator) technology. By using its technology, the sensor and readout ASIC can be prepared in the same wafer. In addition, it realizes high speed, lower power, thin device and low material. Since it is necessary to check the radiation tolerance, noise properties and characteristics of heat discharge, the prototype ASIC is developed. For the first production, we developed only the part of the readout ASIC, which was produced with OKI 0.2 μm FD-SOI CMOS process. The performance of the prototype ASIC will be studied.

6. Acknowledgments

This work is supported by the Commission of the European Communities under the 6^{th} Framework Program "Structuring the European Research Area", contract number RII3-026126. Tsukuba University is supported in part by the Creative Scientific Research Grant No. 18GS0202 of the Japan Society for Promotion of Science. The UST is supported by the Polish Ministry of Science and Higher Education under contract nr 372/6.PRUE/2007/7. IFIN-HH is supported by the Romanian Ministry of Education, research and Innovation through the Authoroty CNCSIS under contract IDEI-253/2007.

References

[1] H. Abramowicz *et al.*., *Instrumentation of the very forward region of a linear collider detector*, *IEEE Trans.Nucl.Sci.***51** (2004) 2983.

[2] K. Mönig, *Physics Needs for the Forward Region*, *V. Workshop: Instrumentation of the Forward Region of a Linear Collider Detector*, August, 26–28, 2004 DESY, Zeuthen, Germany, .

[3] Ch. Grah and A. Sapronov, *Beam parameter determination using beamstrahlung photons and incoherent pairs*, 2008 *JINST* **3** P10004.

[4] S. Agostinelli *et al.*, *Geant4- a simulation toolkit*, *Nucl. Inst. and Meth.A***506** (2003) 250.

[5] MOKKA, A simulation program for linear collider detectors.

[6] T. C. Awes *et al.*., *A simple method of shower localization and identification in laterally segmented calorimeters*, *Nucl. Inst. Meth. A311, 130 (1992)*.

[7] I. Sadeh, *Luminosity Measurement at the International Linear Collider.* , 2008.

[8] H. Abramowicz *et al.*., *Redefinition of the Geometry of the Luminosity Calorimeter*,*EUDET-Memo-2008-09*, 2008. .

[9] J. Brau *et al.*., *ILC Reference Design Report*, , (2007).

[10] D. Schulte, *Beam-beam simulations with guinea-pig*, *CERN-PS-99-014LPCLIC-Note 387* (1998).

[11] A. Seryi, Anti-DID field.

[12] P. Bambade *et al.*., *The Impact of Beamcal Performance at Different ILC Beam Parameters and Crossing Angles on stau Searches*, *Pramana J. Phys.* (2007) 69:1123.

[13] A. Heikkinen and N. Stepanov, *Bertini Intra-nuclear Cascade implementation in Geant4*, *Proceedings of CHEP03*, La Jolla, California, (2003), nucl-th0306008.

[14] C. Coca *et al.*., *Rom. J. Phys., 2010, in press.*

[15] T. Tauchi *et al.*., *Nanometer Beam-Size Measurement during Collisions at Linear Colliders*, *KEK preprint* **94-122** (1995).

[16] T. Tauchi *et al.*., *Pair creation from beam-beam interaction in linear colliders*, *Particle Accelerator* **41**,(1993), 29.

[17] K.Ito, *Study of Beam Profile Measurement at Interaction Point in International Linear Collider*,

[18] C. Rimbault *et al.*. Impact of beam-beam effects on precision luminosity measurements at the ILC. *JINST* , 2 P09001, 2007.

[19] F.A. Berends *et al.*. Monte Carlo simulation of two-photon processes II: Complete lowest order calculations for four-lepton production processes in electron-positron collisions. Comp. Phys. Commun., 40 (1986), pp. 285-307.

[20] W. Kilian. WHIZARD: A generic Monte-Carlo integration and event generation package for multi-particle processes. LC-TOOL-2001-039, 2001.

[21] S. Jadach *et al.*. Monte Carlo program BHLUMI for Bhabha scattering at low polar angle with Yennie-Frautschi-Suura exponentiation. Comp. Phys. Commun., 70 (1992), pp. 305-344.

[22] B. Pawlik. BARBIE V4.3 Easy-to-use-simulation-package of the TESLA LAT Detector , source available from Bogdan.Pawlik@ifj.edu.pl

[23] Ch. Grah *et al.*., *Polycrystalline CVD Diamonds for the Beam Calorimeter of the ILC*, *IEEE Trans.Nucl.Sci.* **56** (2009) 462.

[24] Ch. Grah *et al.*. *Radiation hard sensor for the beamcal of the ILD detector*, *Proceedings of the IEEE conference*, October 27 – November 3 2007 Honolulu, USA.

[25] M.Idzik *et al.*., *Status of LumiCal Readout Electronics*, *EUDET-Report-2008-08*, (2008), .

[26] T.Behnke *et al.*. *TESLA Technical Design Report, PART IV, A Detector for TESLA*, (2001).

[27] M. Idzik *et al.*., *Status of VFCAL*, *EUDET-memo-2008-01* (2008).

[28] M. Idzik *et al.*., *Development of front-end electronics for the luminoisty detector at ILC*, *Nucl. Instr. and Meth.*, in print.

[29] M. Idzik *et al.*., *Development of Pipeline ADC for the Luminosity Detector at ILC*, *Proceedings of the 15th International Conference "Mixed Design of Integrated Circuits and Systems" MIXDES 2008*, Poznan, Poland, 19-21 June (2008).

[30] E. Beuville *et al.*., *AMPLEX, a low-noise, low-power analog CMOS signal processor for multielement silicon particle detectors*, *Nucl. Instr. and Meth.*, A288 1990, 157-167.

[31] G. Gramegna *et al.*., *CMOS preamplifier for low-capacitance detectors*, *Nucl. Instr. and Meth.*, A390 1997, 241-250.

[32] *IEEE standard for terminology and test methods for analog-to-digital converters*, *IEEE-STD-1241* (2000).

[33] J.L. McCreary and P.R. Gray. All-MOS charge redistribution analog-to-digital conversion techniques. I. *Solid-State Circuits, IEEE Journal of*, 10(6):371–379, 1975.

[34] H. Spieler. *Semiconductor Detector Systems*. Oxford University Press, 2005.

[35] R. Gregorian, K.W. Martin, and G.C. Temes. Switched-capacitor circuit design. *Proceedings of the IEEE*, 71(8):941–966, Aug. 1983.

[36] F. Silveira, D. Flandre, and P.G.A. Jespers. A g_m/I_D based methodology for the design of CMOS analog circuits and its application to the synthesis of a silicon-on-insulator micropower OTA. *Solid-State Circuits, IEEE Journal of*, 31(9):1314–1319, 1996.

[37] S. Rabii. *Design of Low-Voltage Low-Power Sigma-Delta Modulators*. PhD thesis, Stanford University, 1998.